Supplementary Materials for

Cryo-EM structure of the 2019-nCoV spike in the prefusion conformation

Daniel Wrapp*, Nianshuang Wang*, Kizzmekia S. Corbett, Jory A. Goldsmith,
Ching-Lin Hsieh, Olubukola Abiona, Barney S. Graham, Jason S. McLellan†

*These authors contributed equally to this work.
†Corresponding author. Email: jmclellan@austin.utexas.edu

Published 19 February 2020 on *Science* First Release
DOI: 10.1126/science.abb2507

This PDF file includes:

Other Supplementary Material for this manuscript includes the following:
(available at science.sciencemag.org/cgi/content/full/science.abb2507/DC1)

Materials and Methods

Protein expression and purification

To express the prefusion S ectodomain, a gene encoding residues 1–1208 of 2019-nCoV S (GenBank: MN908947) with proline substitutions at residues 986 and 987, a "GSAS" substitution at the furin cleavage site (residues 682–685), a C-terminal T4 fibritin trimerization motif, an HRV3C protease cleavage site, a TwinStrepTag and an 8XHisTag was synthesized and cloned into the mammalian expression vector pαH. To express the 2019-nCoV RBD-SD1, residues 319–591 of 2019-nCoV S were cloned upstream of a C-terminal HRV3C protease cleavage site, a monomeric Fc tag and an 8XHisTag. Similarly, to express the SARS-CoV RBD-SD1, residues 306–577 of SARS-CoV S (Tor2 strain) were cloned upstream of a C-terminal HRV3C protease cleavage site, a monomeric Fc tag and an 8XHisTag. Lastly, a plasmid encoding residues 1–615 of human ACE2 with a C-terminal HRV3C protease cleavage site, a TwinStrepTag and an 8XHisTag was generated.

These expression vectors were used to transiently transfect FreeStyle293F cells (Thermo Fisher) using polyethylenimine. Protein was purified from filtered cell supernatants using either StrepTactin resin (IBA) or Protein A resin (Pierce) before being subjected to additional purification by size-exclusion chromatography using either a Superose 6 10/300 column (GE Healthcare) or a Superdex 200 10/300 Increase column (GE Healthcare) in 2 mM Tris pH 8.0, 200 mM NaCl and 0.02% NaN_3. ACE2 and the 2019-nCoV RBD-SD1 were incubated with 10% (wt/wt) HRV3C protease for 2 hours at room temperature. Cleaved protein was then passed over either NiNTA resin (ACE2) or Protein A and NiNTA resins (2019-nCoV RBD-SD1) to remove cleaved tags and His-tagged protease before being run over a Superdex 200 10/300 Increase column in 2 mM Tris pH 8.0, 200 mM NaCl and 0.02% NaN_3.

Plasmids encoding the heavy and light chains of S230, 80R and m396 IgG were transiently transfected into Expi293 cells (Thermo Fisher) using polyethylenimine. Antibodies were purified from cell supernatants using Protein A resin before being used for biolayer interferometry.

Cryo-EM sample preparation and data collection

Purified 2019-nCoV S was diluted to a concentration of 0.35 mg/mL in 2 mM Tris pH 8.0, 200 mM NaCl and 0.02% NaN_3. 3 uL of protein was deposited on a CF-1.2/1.3 grid that had been plasma cleaned for 30 seconds in a Solarus 950 plasma cleaner (Gatan) with a 4:1 ratio of O_2/H_2. Excess protein was blotted away for 6 seconds using grade 595 vitrobot filter paper (Ted Pella Inc.) with a force of -1 at 4 °C in 100% humidity before being plunge frozen into liquid ethane using a Vitrobot Mark IV (Thermo Fisher). Frozen grids were imaged in a Titan Krios (Thermo Fisher) equipped with a K3 detector (Gatan). Movies were collected using Leginon (*32*) at a magnification of x22,500, corresponding to a calibrated pixel size of 1.047 Å/pixel. A full description of the cryo-EM data collection parameters can be found in **table S1**.

Cryo-EM data processing

Motion correction, CTF-estimation and non-templated particle picking were performed in Warp (*33*). Extracted particles were imported into cryoSPARC v2.12.4 (*15*) for 2D classification, 3D classification and non-uniform 3D refinement. The C1 RBD-up reconstruction was sharpened in cryoSPARC, and the 3D reconstruction with C3 symmetry was subjected to local B-factor sharpening using LocalDeBlur (*34*). An initial 2019-nCoV S model was generated from PDBID: 6CRZ (*14*) using Modeller (*35*) via UCSF Chimera (*36*). The model was further built manually in Coot, using PDBID: 6NB6 (*12*) to aid secondary structure placement, before being iteratively refined in both Phenix and ISOLDE (*37-39*). Phenix refinement strategy included minimization_global, local_grid_search, and adp, with rotamer, Ramachandran, and reference-model restraints, using 6NB6 as the reference model. Some of the data processing and refinement software was curated by SBGrid (*40*). The full cryo-EM data processing workflow is described in **fig. S3** and the model refinement statistics can be found in **table S1**.

Surface plasmon resonance

His-tagged 2019-nCoV S was immobilized to an NiNTA sensorchip (GE Healthcare) to a level of ~800 response units (RUs) using a Biacore X100 (GE Healthcare) and a running buffer composed of 10 mM HEPES pH 8.0, 150 mM NaCl and 0.05% Tween 20. Serial dilutions of purified and untagged ACE2

were injected ranging in concentration from 250 to 15.6 nM. The resulting data were fit to a 1:1 binding model using Biacore Evaluation Software (GE Healthcare). His-tagged SARS-CoV RBD-SD1 was immobilized to an NiNTA sensorchip to a level of ~350 RUs using a Biacore X100 and the same running buffer listed above. Serial dilutions of purified and untagged ACE2 were injected ranging in concentration from 500 to 31.3 nM. The resulting data were fit to a 1:1 binding model using Biacore Evaluation Software.

Negative stain EM

Purified 2019-nCoV S was diluted to a concentration of 0.032 mg/mL in 2 mM Tris pH 8.0, 200 mM NaCl and 0.02% NaN_3. Diluted S protein was mixed with a 1.5-fold molar excess of ACE2 and the mixture was incubated on ice for 1 minute before 4.8 uL of the protein mixture was deposited on a CF400-Cu grid (Electron Microscopy Sciences) before being stained with methylamine tungstate (Nanoprobes). This grid was imaged in an FEI Talos TEM (Thermo Scientific) equipped with a Ceta 16M detector. Micrographs were collected manually using TIA v4.14 software at a magnification of x92,000, corresponding to a pixel size of 1.63 Å/pixel. CTF estimation, particle picking and 2D class averaging were performed in *cis*TEM (*41*).

Biolayer interferometry

Fc-tagged 2019-nCoV RBD-SD1 was immobilized to an anti-human capture (AHC) sensortip (FortéBio) using an Octet RED96e (FortéBio). The sensortip was then dipped into 100 nM ACE2 to measure association before being dipped into a well containing only running buffer composed of 10 mM HEPES pH 7.5, 150 mM NaCl, 3 mM EDTA, 0.05% Tween 20 and 1 mg/mL bovine serum albumin to measure dissociation. Data were reference subtracted and fit to a 1:1 binding model using Octet Data Analysis Software v11.1 (FortéBio).

S230, 80R and m396 IgGs were immobilized to AHC sensortips to a response level of ~0.8 nm and dipped into wells containing 1 μM untagged 2019-nCoV RBD-SD1 before being dipped into wells

containing only running buffer to measure dissociation. Data were reference-subtracted and aligned to a baseline after IgG capture using Octet Data Analysis software v11.1. An analogous experiment was performed under identical conditions by dipping AHC sensor tips loaded with S230, 80R or m396 IgG into untagged SARS-CoV RBD-SD1. Data were reference-subtracted, aligned to a baseline after IgG capture and fit to a 1:1 binding model using Octet Data Analysis software v11.1.

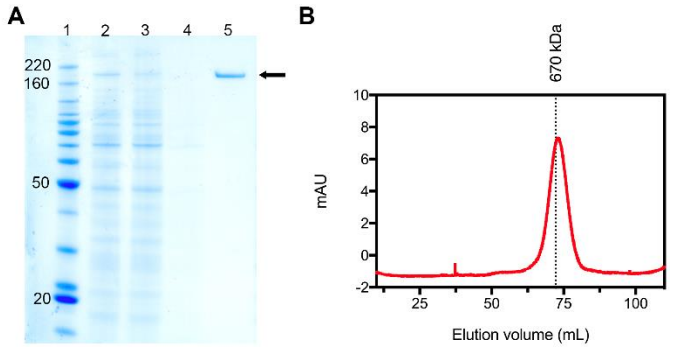

Figure S1. 2019-nCoV S expression and purification. (**A**) SDS-PAGE analysis of the 2019-nCoV S protein. Lane 1: molecular weight ladder, with relevant bands labeled in kilodaltons (*left*); lane 2: filtered supernatant from transfected cells; lane 3: supernatant after passing through StrepTactin resin; lane 4: wash of StrepTactin resin; lane 5: elution from StrepTactin resin. The band corresponding to 2019-nCoV S is denoted with a black arrow. (**B**) Size-exclusion chromatogram of the affinity-purified 2019-nCoV S protein. Data from a Superose 6 10/300 column are shown in red. The elution volume of a 670 kilodalton molecular weight standard is shown as a black dotted line.

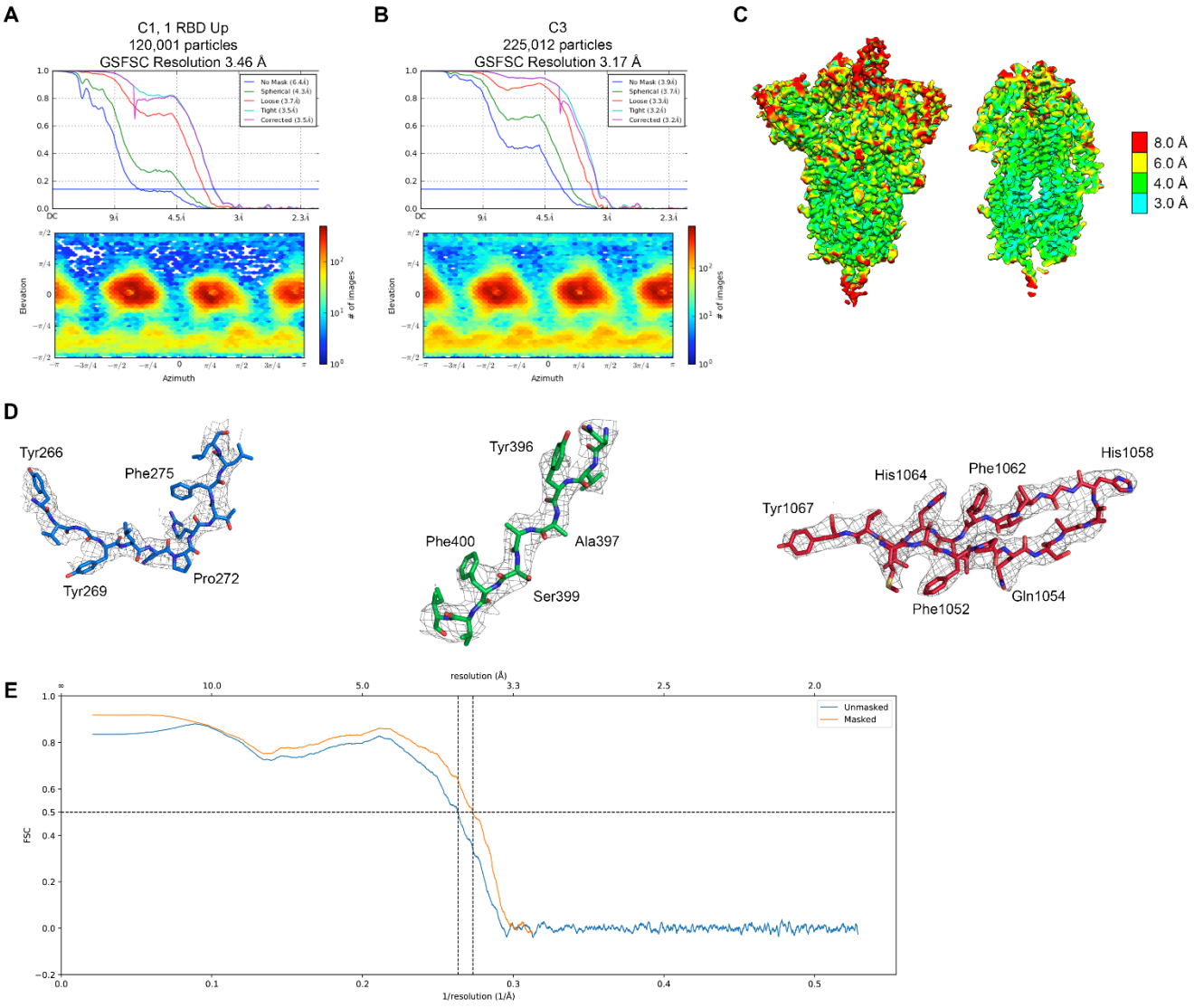

Figure S2. Cryo-EM structure validation. (**A**) FSC curves (*top*) and the viewing direction distribution plot (*bottom*) for 2019-nCoV S with a single RBD up. (**B**) FSC curves (*top*) and the viewing direction distribution plot (*bottom*) for the 2019-nCoV S processed with C3 symmetry. (**C**) Cryo-EM density of the 2019-nCoV S with a single RBD up is shown, colored according to local resolution. Image on the right is a central slice through the density. (**D**) Density and corresponding model from portions of the NTD (blue), RBD (green), and S2 (red). Residues are shown as sticks, colored according to **Fig. 1A** with oxygen atoms colored red, nitrogen blue and sulfur yellow. Cryo-EM density map is shown as a gray mesh. (E) Model-to-map FSC.

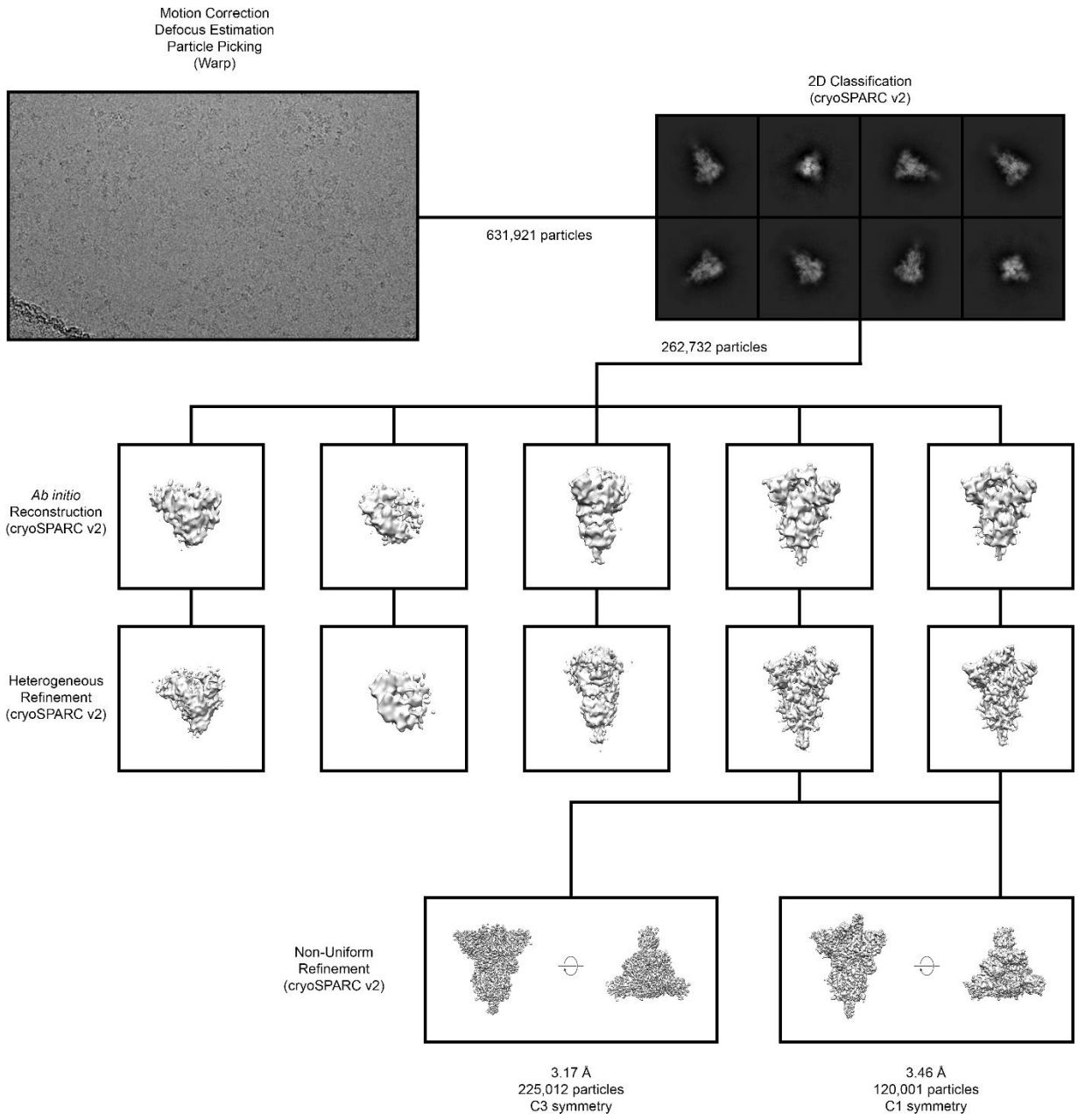

Figure S3. Cryo-EM data processing workflow.

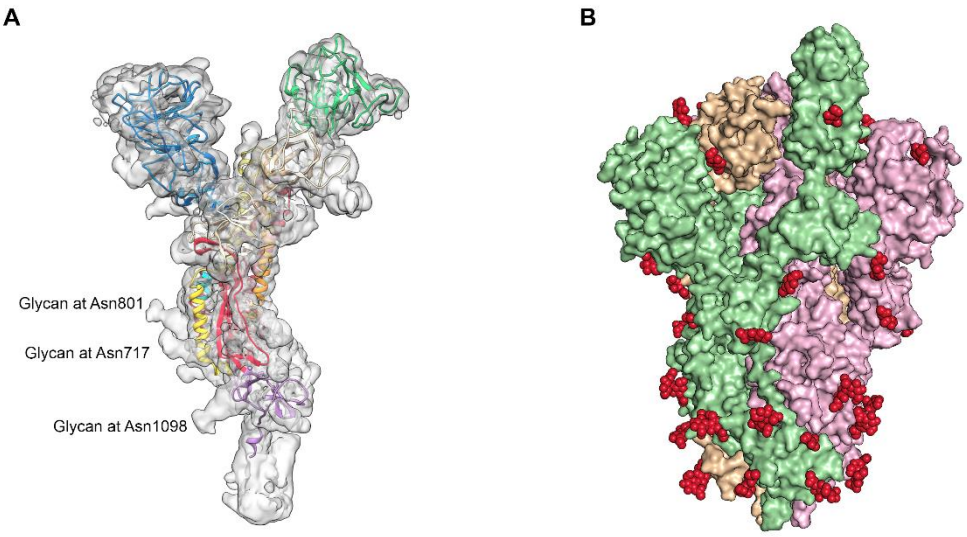

Figure S4. Cryo-EM map and *N*-linked glycosylation sites. (**A**) The asymmetric unit of the unsharpened cryo-EM density map for the C3-processed 2019-nCoV S is shown as a transparent molecular surface, with a single protomer fit into the map shown in ribbons and colored according to **Fig. 1A**. Some of the S2 density that corresponds to *N*-linked glycans is labeled. (**B**) The 2019-nCoV S trimer with a single RBD up is shown as a molecular surface with each protomer colored green, pink or tan. Modeled *N*-linked glycans are shown as red spheres.

Figure S5. Sequence alignment of 2019-nCoV S, SARS-CoV S and RaTG13 S. Identical residues are denoted by an "*" beneath the consensus position. Structural domains are colored according to **Fig. 1A**.

A

Domain	Variant residues
NTD	Phe32, Ser50, Thr76, Gln218
RBD	Arg346, Ala372, Arg403, Asn439, Asn440, Leu441, Ser443, Val445, Tyr449, Ser459, Thr478, Val483, Glu484, Phe486, Phe490, Gln493, Ser494, Gln498, Asn501, Tyr505, His519
SD1	Glu324
SD2	Thr604
S1/S2	682-PRRA-685 (insertion)
S2	Asn1125, Val1228

B

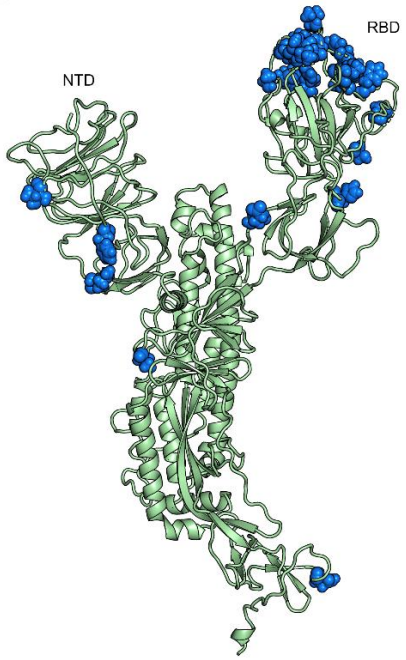

C

Domain	Substitution	2019-nCoV isolates
NTD	F32I	IVDC-HB-01/2019
	H49Y	20SF028/2020, 20SF040/2020, 20SF174/2020
	S247R	VIC01/2020
RBD	N354D	SZTH-004/2020
	D364Y	SZTH-004/2020
	V367F	IDF0372/2020, IDF0373/2020
SD2	D614G	BavPat1/2020
S2	V1129L	SZTH-001/2020
	E1262G	SZTH-001/2020

D

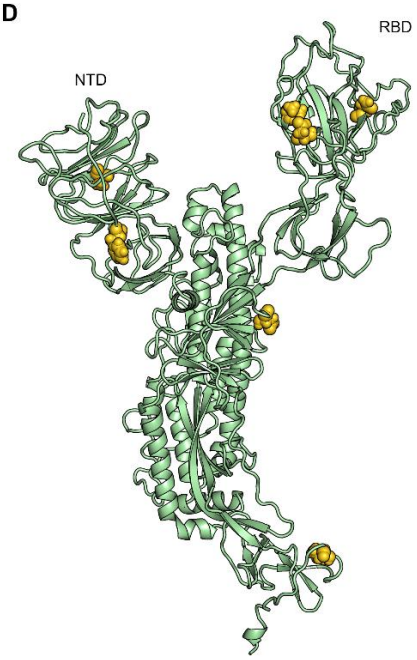

Figure S6. Sequence variability between RaTG13 S and 2019-nCoV S clinical isolates. (**A**) Table shows residues in the 2019-nCoV S protein that vary in RaTG13, grouped by structural domain. (**B**) A single RBD-down protomer of the 2019-nCoV S protein is shown in ribbons, colored green. RaTG13 variant residues are shown as blue spheres. (**C**) Table shows variations in the 2019-nCoV S sequence based on 61 clinical isolates and the domains wherein these variations occur. (**D**) A single RBD-down protomer of the 2019-nCoV S protein is shown in ribbons, colored green. Variant residues are shown as gold spheres.

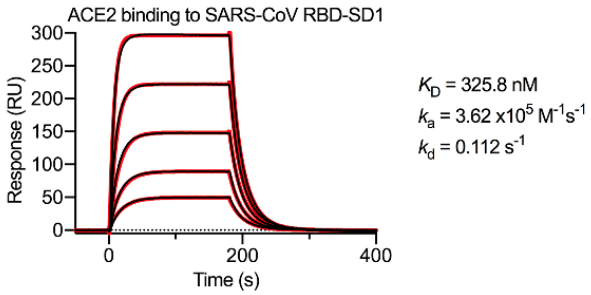

Figure S7. SARS-CoV RBD-SD1 binding to human ACE2. An SPR sensorgram is shown, displaying the binding between soluble human ACE2 and immobilized SARS-CoV RBD-SD1. The data are shown as black lines and the best fit of the data to a 1:1 binding model is shown in red.

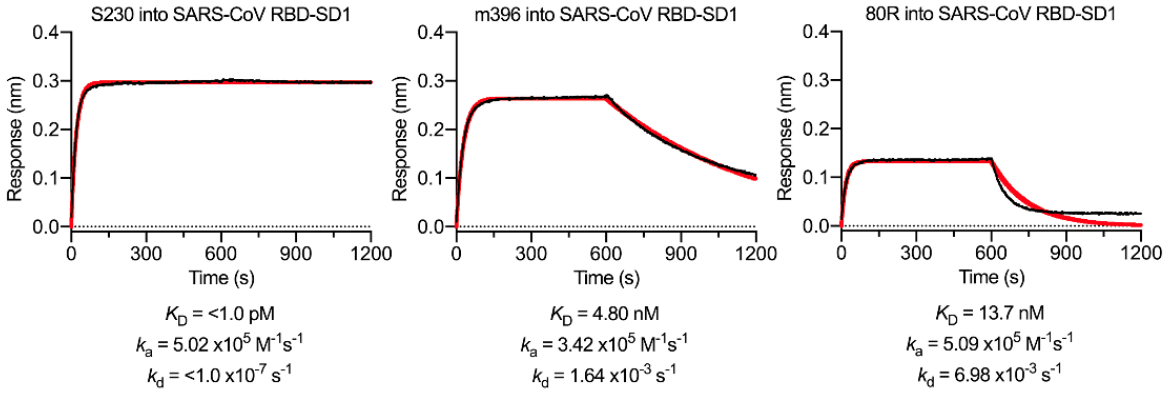

Figure S8. SARS-CoV RBD-directed antibody validation. The monoclonal antibodies that were tested for cross-reactivity to the 2019-nCoV RBD-SD1 were also tested for binding to the SARS-CoV S RBD-SD1 as a positive control. Binding data are shown as a black line and the best fit of the data to a 1:1 binding model is shown in red.

Table S1. Cryo-EM data collection and refinement statistics.

EM data collection and reconstruction statistics		
Protein	2019-nCoV S One RBD up	2019-nCoV S C3 symmetry
EMDB	EMD-21375	EMD-21374
Microscope	FEI Titan Krios	FEI Titan Krios
Voltage (kV)	300	300
Detector	Gatan K3	Gatan K3
Magnification (nominal)	22,500	22,500
Pixel size (Å/pix)	1.047	1.047
Flux (e^-/pix/sec)	8.0	8.0
Frames per exposure	30	30
Exposure (e^-/Å^2)	36	36
Defocus range (μm)	0.8–2.8	0.8–2.8
Micrographs collected	3,207	3,207
Particles extracted/final	631,921/120,001	631,921/225,012
Symmetry imposed	n/a (C1)	C3
Map sharpening B-factor	-78.8	n/a (LocalDeBlur)
Unmasked resolution at 0.5/0.143 FSC (Å)	4.22/3.89	6.90/3.95
Masked resolution at 0.5/0.143 FSC (Å)	3.85/3.46	3.45/3.17

Model refinement and validation statistics	
PDB	6VSB
Composition	
Amino acids	2,905
Glycans	61
RMSD bonds (Å)	0.004
RMSD angles (º)	0.88
Mean B-factors	
Amino acids	109.5
Glycans	119.6
Ramachandran	
Favored (%)	94.6
Allowed (%)	5.2
Outliers (%)	0.2
Rotamer outliers (%)	0.64
Clash score	12.8
C-beta outliers (%)	0.0
CaBLAM outliers (%)	3.11
CC (mask)	0.82
MolProbity score	1.99
EMRinger score	2.06

Movie S1. CryoSPARC 3D variability analysis side-view. 2019-nCoV S trimer viewed from the side, along the viral membrane.

Movie S2. CryoSPARC 3D variability analysis top-view. 2019-nCoV S trimer viewed from the top, toward the viral membrane.

References and Notes

1. J. F. Chan, S. Yuan, K.-H. Kok, K. K.-W. To, H. Chu, J. Yang, F. Xing, J. Liu, C. C.-Y. Yip, R. W.-S. Poon, H.-W. Tsoi, S. K.-F. Lo, K.-H. Chan, V. K.-M. Poon, W.-M. Chan, J. D. Ip, J.-P. Cai, V. C.-C. Cheng, H. Chen, C. K.-M. Hui, K.-Y. Yuen, A familial cluster of pneumonia associated with the 2019 novel coronavirus indicating person-to-person transmission: A study of a family cluster. *Lancet* **395**, 514–523 (2020). doi:10.1016/S0140-6736(20)30154-9 Medline

2. C. Huang, Y. Wang, X. Li, L. Ren, J. Zhao, Y. Hu, L. Zhang, G. Fan, J. Xu, X. Gu, Z. Cheng, T. Yu, J. Xia, Y. Wei, W. Wu, X. Xie, W. Yin, H. Li, M. Liu, Y. Xiao, H. Gao, L. Guo, J. Xie, G. Wang, R. Jiang, Z. Gao, Q. Jin, J. Wang, B. Cao, Clinical features of patients infected with 2019 novel coronavirus in Wuhan, China. *Lancet* **395**, 497–506 (2020). doi:10.1016/S0140-6736(20)30183-5 Medline

3. R. Lu, X. Zhao, J. Li, P. Niu, B. Yang, H. Wu, W. Wang, H. Song, B. Huang, N. Zhu, Y. Bi, X. Ma, F. Zhan, L. Wang, T. Hu, H. Zhou, Z. Hu, W. Zhou, L. Zhao, J. Chen, Y. Meng, J. Wang, Y. Lin, J. Yuan, Z. Xie, J. Ma, W. J. Liu, D. Wang, W. Xu, E. C. Holmes, G. F. Gao, G. Wu, W. Chen, W. Shi, W. Tan, Genomic characterisation and epidemiology of 2019 novel coronavirus: Implications for virus origins and receptor binding. *Lancet* S0140-6736(20)30251-8 (2020). doi:10.1016/S0140-6736(20)30251-8 Medline

4. F. Wu, S. Zhao, B. Yu, Y.-M. Chen, W. Wang, Z.-G. Song, Y. Hu, Z.-W. Tao, J.-H. Tian, Y.-Y. Pei, M.-L. Yuan, Y.-L. Zhang, F.-H. Dai, Y. Liu, Q.-M. Wang, J.-J. Zheng, L. Xu, E. C. Holmes, Y.-Z. Zhang, A new coronavirus associated with human respiratory disease in China. *Nature* (2020). doi:10.1038/s41586-020-2008-3 Medline

5. N. Chen, M. Zhou, X. Dong, J. Qu, F. Gong, Y. Han, Y. Qiu, J. Wang, Y. Liu, Y. Wei, J. Xia, T. Yu, X. Zhang, L. Zhang, Epidemiological and clinical characteristics of 99 cases of 2019 novel coronavirus pneumonia in Wuhan, China: A descriptive study. *Lancet* **395**, 507–513 (2020). doi:10.1016/S0140-6736(20)30211-7 Medline

6. Q. Li, X. Guan, P. Wu, X. Wang, L. Zhou, Y. Tong, R. Ren, K. S. M. Leung, E. H. Y. Lau, J. Y. Wong, X. Xing, N. Xiang, Y. Wu, C. Li, Q. Chen, D. Li, T. Liu, J. Zhao, M. Li, W. Tu, C. Chen, L. Jin, R. Yang, Q. Wang, S. Zhou, R. Wang, H. Liu, Y. Luo, Y. Liu, G. Shao, H. Li, Z. Tao, Y. Yang, Z. Deng, B. Liu, Z. Ma, Y. Zhang, G. Shi, T. T. Y. Lam, J. T. K. Wu, G. F. Gao, B. J. Cowling, B. Yang, G. M. Leung, Z. Feng, Early Transmission Dynamics in Wuhan, China, of Novel Coronavirus-Infected Pneumonia. *N. Engl. J. Med.* NEJMoa2001316 (2020). doi:10.1056/NEJMoa2001316 Medline

7. F. Li, Structure, Function, and Evolution of Coronavirus Spike Proteins. *Annu. Rev. Virol.* **3**, 237–261 (2016). doi:10.1146/annurev-virology-110615-042301 Medline

8. B. J. Bosch, R. van der Zee, C. A. de Haan, P. J. Rottier, The coronavirus spike protein is a class I virus fusion protein: Structural and functional characterization of the fusion core complex. *J. Virol.* **77**, 8801–8811 (2003). doi:10.1128/JVI.77.16.8801-8811.2003 Medline

9. A. C. Walls, M. A. Tortorici, J. Snijder, X. Xiong, B.-J. Bosch, F. A. Rey, D. Veesler, Tectonic conformational changes of a coronavirus spike glycoprotein promote membrane

fusion. *Proc. Natl. Acad. Sci. U.S.A.* **114**, 11157–11162 (2017). doi:10.1073/pnas.1708727114 Medline

10. M. Gui, W. Song, H. Zhou, J. Xu, S. Chen, Y. Xiang, X. Wang, Cryo-electron microscopy structures of the SARS-CoV spike glycoprotein reveal a prerequisite conformational state for receptor binding. *Cell Res.* **27**, 119–129 (2017). doi:10.1038/cr.2016.152 Medline

11. J. Pallesen, N. Wang, K. S. Corbett, D. Wrapp, R. N. Kirchdoerfer, H. L. Turner, C. A. Cottrell, M. M. Becker, L. Wang, W. Shi, W.-P. Kong, E. L. Andres, A. N. Kettenbach, M. R. Denison, J. D. Chappell, B. S. Graham, A. B. Ward, J. S. McLellan, Immunogenicity and structures of a rationally designed prefusion MERS-CoV spike antigen. *Proc. Natl. Acad. Sci. U.S.A.* **114**, E7348–E7357 (2017). doi:10.1073/pnas.1707304114 Medline

12. A. C. Walls, X. Xiong, Y.-J. Park, M. A. Tortorici, J. Snijder, J. Quispe, E. Cameroni, R. Gopal, M. Dai, A. Lanzavecchia, M. Zambon, F. A. Rey, D. Corti, D. Veesler, Unexpected receptor functional mimicry elucidates activation of coronavirus fusion. *Cell* **176**, 1026–1039.e15 (2019). doi:10.1016/j.cell.2018.12.028 Medline

13. Y. Yuan, D. Cao, Y. Zhang, J. Ma, J. Qi, Q. Wang, G. Lu, Y. Wu, J. Yan, Y. Shi, X. Zhang, G. F. Gao, Cryo-EM structures of MERS-CoV and SARS-CoV spike glycoproteins reveal the dynamic receptor binding domains. *Nat. Commun.* **8**, 15092 (2017). doi:10.1038/ncomms15092 Medline

14. R. N. Kirchdoerfer, N. Wang, J. Pallesen, D. Wrapp, H. L. Turner, C. A. Cottrell, K. S. Corbett, B. S. Graham, J. S. McLellan, A. B. Ward, Stabilized coronavirus spikes are resistant to conformational changes induced by receptor recognition or proteolysis. *Sci. Rep.* **8**, 15701 (2018). doi:10.1038/s41598-018-34171-7 Medline

15. A. Punjani, J. L. Rubinstein, D. J. Fleet, M. A. Brubaker, cryoSPARC: Algorithms for rapid unsupervised cryo-EM structure determination. *Nat. Methods* **14**, 290–296 (2017). doi:10.1038/nmeth.4169 Medline

16. D. Wrapp, J. S. McLellan, The 3.1-angstrom cryo-electron microscopy structure of the porcine epidemic diarrhea virus spike protein in the prefusion conformation. *J. Virol.* **93**, e00923-19 (2019). doi:10.1128/JVI.00923-19 Medline

17. A. C. Walls, M. A. Tortorici, B. Frenz, J. Snijder, W. Li, F. A. Rey, F. DiMaio, B.-J. Bosch, D. Veesler, Glycan shield and epitope masking of a coronavirus spike protein observed by cryo-electron microscopy. *Nat. Struct. Mol. Biol.* **23**, 899–905 (2016). doi:10.1038/nsmb.3293 Medline

18. R. N. Kirchdoerfer, C. A. Cottrell, N. Wang, J. Pallesen, H. M. Yassine, H. L. Turner, K. S. Corbett, B. S. Graham, J. S. McLellan, A. B. Ward, Pre-fusion structure of a human coronavirus spike protein. *Nature* **531**, 118–121 (2016). doi:10.1038/nature17200 Medline

19. B. Coutard, C. Valle, X. de Lamballerie, B. Canard, N. G. Seidah, E. Decroly, The spike glycoprotein of the new coronavirus 2019-nCoV contains a furin-like cleavage site absent in CoV of the same clade. *Antiviral Res.* **176**, 104742 (2020). doi:10.1016/j.antiviral.2020.104742 Medline

20. B. J. Bosch, W. Bartelink, P. J. Rottier, Cathepsin L functionally cleaves the severe acute respiratory syndrome coronavirus class I fusion protein upstream of rather than adjacent to the fusion peptide. *J. Virol.* **82**, 8887–8890 (2008). doi:10.1128/JVI.00415-08 Medline

21. I. Glowacka, S. Bertram, M. A. Müller, P. Allen, E. Soilleux, S. Pfefferle, I. Steffen, T. S. Tsegaye, Y. He, K. Gnirss, D. Niemeyer, H. Schneider, C. Drosten, S. Pöhlmann, Evidence that TMPRSS2 activates the severe acute respiratory syndrome coronavirus spike protein for membrane fusion and reduces viral control by the humoral immune response. *J. Virol.* **85**, 4122–4134 (2011). doi:10.1128/JVI.02232-10 Medline

22. W. Li, M. J. Moore, N. Vasilieva, J. Sui, S. K. Wong, M. A. Berne, M. Somasundaran, J. L. Sullivan, K. Luzuriaga, T. C. Greenough, H. Choe, M. Farzan, Angiotensin-converting enzyme 2 is a functional receptor for the SARS coronavirus. *Nature* **426**, 450–454 (2003). doi:10.1038/nature02145 Medline

23. S. Belouzard, V. C. Chu, G. R. Whittaker, Activation of the SARS coronavirus spike protein via sequential proteolytic cleavage at two distinct sites. *Proc. Natl. Acad. Sci. U.S.A.* **106**, 5871–5876 (2009). doi:10.1073/pnas.0809524106 Medline

24. J. Chen, K. H. Lee, D. A. Steinhauer, D. J. Stevens, J. J. Skehel, D. C. Wiley, Structure of the hemagglutinin precursor cleavage site, a determinant of influenza pathogenicity and the origin of the labile conformation. *Cell* **95**, 409–417 (1998). doi:10.1016/S0092-8674(00)81771-7 Medline

25. M. Hoffmann, H. Kleine-Weber, N. Krüger, M. Müller, C. Drosten, S. Pöhlmann, The novel coronavirus 2019 (2019-nCoV) uses the SARS-coronavirus receptor ACE2 and the cellular protease TMPRSS2 for entry into target cells. bioRxiv 929042 [Preprint]. 31 January 2020. https://doi.org/10.1101/2020.01.31.929042.

26. Y. Wan, J. Shang, R. Graham, R. S. Baric, F. Li, Receptor recognition by novel coronavirus from Wuhan: An analysis based on decade-long structural studies of SARS. *J. Virol.* JVI.00127-20 (2020). doi:10.1128/JVI.00127-20 Medline

27. P. Zhou, X.-L. Yang, X.-G. Wang, B. Hu, L. Zhang, W. Zhang, H.-R. Si, Y. Zhu, B. Li, C.-L. Huang, H.-D. Chen, J. Chen, Y. Luo, H. Guo, R.-D. Jiang, M.-Q. Liu, Y. Chen, X.-R. Shen, X. Wang, X.-S. Zheng, K. Zhao, Q.-J. Chen, F. Deng, L.-L. Liu, B. Yan, F.-X. Zhan, Y.-Y. Wang, G.-F. Xiao, Z.-L. Shi, A pneumonia outbreak associated with a new coronavirus of probable bat origin. *Nature* (2020). doi:10.1038/s41586-020-2012-7 Medline

28. W. Song, M. Gui, X. Wang, Y. Xiang, Cryo-EM structure of the SARS coronavirus spike glycoprotein in complex with its host cell receptor ACE2. *PLOS Pathog.* **14**, e1007236 (2018). doi:10.1371/journal.ppat.1007236 Medline

29. W. C. Hwang, Y. Lin, E. Santelli, J. Sui, L. Jaroszewski, B. Stec, M. Farzan, W. A. Marasco, R. C. Liddington, Structural basis of neutralization by a human anti-severe acute respiratory syndrome spike protein antibody, 80R. *J. Biol. Chem.* **281**, 34610–34616 (2006). doi:10.1074/jbc.M603275200 Medline

30. P. Prabakaran, J. Gan, Y. Feng, Z. Zhu, V. Choudhry, X. Xiao, X. Ji, D. S. Dimitrov, Structure of severe acute respiratory syndrome coronavirus receptor-binding domain

complexed with neutralizing antibody. *J. Biol. Chem.* **281**, 15829–15836 (2006). doi:10.1074/jbc.M600697200 Medline

31. X. Tian, C. Li, A. Huang, S. Xia, S. Lu, Z. Shi, L. Lu, S. Jiang, Z. Yang, Y. Wu, T. Ying, Potent binding of 2019 novel coronavirus spike protein by a SARS coronavirus-specific human monoclonal antibody. *bioRxiv* **9**, 382–385 (2020). doi:10.1080/22221751.2020.1729069

32. B. Carragher, N. Kisseberth, D. Kriegman, R. A. Milligan, C. S. Potter, J. Pulokas, A. Reilein, Leginon: An automated system for acquisition of images from vitreous ice specimens. *J. Struct. Biol.* **132**, 33–45 (2000). doi:10.1006/jsbi.2000.4314 Medline

33. D. Tegunov, P. Cramer, Real-time cryo-electron microscopy data preprocessing with Warp. *Nat. Methods* **16**, 1146–1152 (2019). doi:10.1038/s41592-019-0580-y Medline

34. E. Ramírez-Aportela, J. L. Vilas, A. Glukhova, R. Melero, P. Conesa, M. Martínez, D. Maluenda, J. Mota, A. Jiménez, J. Vargas, R. Marabini, P. M. Sexton, J. M. Carazo, C. O. S. Sorzano, Automatic local resolution-based sharpening of cryo-EM maps. *Bioinformatics* **36**, 765–772 (2020). 10.1093/bioinformatics/btz671 Medline

35. A. Šali, T. L. Blundell, Comparative protein modelling by satisfaction of spatial restraints. *J. Mol. Biol.* **234**, 779–815 (1993). doi:10.1006/jmbi.1993.1626 Medline

36. E. F. Pettersen, T. D. Goddard, C. C. Huang, G. S. Couch, D. M. Greenblatt, E. C. Meng, T. E. Ferrin, UCSF Chimera—A visualization system for exploratory research and analysis. *J. Comput. Chem.* **25**, 1605–1612 (2004). doi:10.1002/jcc.20084 Medline

37. P. D. Adams, R. W. Grosse-Kunstleve, L.-W. Hung, T. R. Ioerger, A. J. McCoy, N. W. Moriarty, R. J. Read, J. C. Sacchettini, N. K. Sauter, T. C. Terwilliger, PHENIX: Building new software for automated crystallographic structure determination. *Acta Crystallogr. D Biol. Crystallogr.* **58**, 1948–1954 (2002). doi:10.1107/S0907444902016657 Medline

38. T. I. Croll, ISOLDE: A physically realistic environment for model building into low-resolution electron-density maps. *Acta Crystallogr. D Struct. Biol.* **74**, 519–530 (2018). doi:10.1107/S2059798318002425 Medline

39. P. Emsley, K. Cowtan, Coot: Model-building tools for molecular graphics. *Acta Crystallogr. D Biol. Crystallogr.* **60**, 2126–2132 (2004). doi:10.1107/S0907444904019158 Medline

40. A. Morin, B. Eisenbraun, J. Key, P. C. Sanschagrin, M. A. Timony, M. Ottaviano, P. Sliz, Collaboration gets the most out of software. *eLife* **2**, e01456 (2013). doi:10.7554/eLife.01456 Medline

41. T. Grant, A. Rohou, N. Grigorieff, *cis*TEM, user-friendly software for single-particle image processing. *eLife* **7**, e35383 (2018). doi:10.7554/eLife.35383 Medline